Exp Fluids (2017) 58:47
DOI 10.1007/s00348-016-2294-6

RESEARCH ARTICLE

Faraday wave patterns on a square cell network

Franklin Peña-Polo[1,2] · Carlos A. Vargas[3] · Benjamín Vásquez-González[4] · Abraham Medina[5] · Leonardo Trujillo[1] · Jaime Klapp[2,6] · Leonardo Di G. Sigalotti[3]

Received: 6 August 2016 / Revised: 13 December 2016 / Accepted: 20 December 2016

Abstract We present the experimental observations of the Faraday instability when the vibrated liquid is contained in a network of small square cells for exciting frequencies in the range $10 \leq F \leq 24$ Hz. A sweep of the parameter space has been performed to investigate the amplitudes and frequencies of the driving force for which different patterns form over the network. Regular patterns in the form of square lattices are observed for driving frequencies in the range $10 \leq F < 14$ Hz, while ordered matrices of oscillons are formed for $14 < F \leq 23$ Hz. At $F > 23$ Hz, disordered periodic patterns appear within individual cells for a small range of amplitudes. In this case, the wave field is dominated by oscillating blobs that interact on the capillary–gravity scale. A Pearson correlation analysis of the recorded videos shows that for all ordered patterns, the surface waves are periodic and correspond to Faraday waves of dominant frequency equal to half the excitation frequency (i.e., $f = F/2$). In contrast, the oscillons formed for $14 < F \leq 23$ Hz are at the first subharmonic ($f = F/2$) and first harmonic ($f = F$) response frequencies, with higher harmonics being negligible or absent as in most cases. The disordered wave fields forming at $F > 23$ Hz are not subharmonic and correspond to periodic harmonic waves with $f = nF/2$ (for $n = 2, 4, \ldots$). We find that the experimentally determined minimum forcing necessary to destabilize the rest state and generate surface waves is consistent with a recent stability analysis of stationary solutions as derived from a new dispersion relation for time-periodic waves with nonzero forcing and dissipation.

✉ Leonardo Di G. Sigalotti
leonardo.sigalotti@gmail.com

[1] Centro de Física, Instituto Venezolano de Investigaciones Científicas (IVIC), Apartado Postal 20632, Caracas 1020, Venezuela

[2] Departamento de Matemáticas, ABACUS-Centro de Matemáticas Aplicadas y Cómputo de Alto Rendimiento, Centro de Investigación y de Estudios Avanzados (Cinvestav-IPN), Carretera México-Toluca Km. 38.5, La Marquesa, 52740 Ocoyoacac, Estado de México, Mexico

[3] Área de Física de Procesos Irreversibles, Departamento de Ciencias Básicas, Universidad Autónoma Metropolitana-Azcapotzalco (UAM-A), Av. San Pablo 180, 02200 Mexico City, DF, Mexico

[4] Departamento de Energía, Universidad Autónoma Metropolitana-Azcapotzalco (UAM-A), Av. San Pablo 180, 02200 Mexico City, DF, Mexico

[5] ESIME-Azcapotzalco, Instituto Politécnico Nacional (IPN), Av. de Las Granjas 682, Colonia Santa Catarina, Azcapotzalco, 02250 Mexico City, DF, Mexico

[6] Departamento de Física, Instituto Nacional de Investigaciones Nucleares (ININ), Carretera México-Toluca km. 36.5, La Marquesa, 52750 Ocoyoacac, Estado de México, Mexico

1 Introduction

When a vessel containing a fluid is submitted to periodic vertical oscillations, standing waves appear on the surface of the fluid for a range of frequencies and amplitudes of the forcing oscillations. These waves, called Faraday waves or standing gravity waves (Faraday 1831; Benjamin and Ursell 1954), are parametrically excited when the vertical oscillations are above a critical frequency, F_c, or critical forcing acceleration, Γ_c. The oscillating parameter is the apparent gravity, which, in the reference frame moving with the vessel, is

$$g(t) = g[1 + \Gamma \cos(\Omega t)], \tag{1}$$

Published online: 03 April 2017

where $\Gamma = A\Omega^2/g$ is the dimensionless forcing, g the acceleration due to gravity in the reference frame of the laboratory, A the amplitude, $\Omega(= 2\pi F)$ the angular frequency, and F the linear frequency of the driving force. Faraday (1831) first noted that the waves that appear on the fluid surface are at the first subharmonic of the excitation frequency, $f = F/2$.

The Faraday instability has been studied extensively over decades, both theoretically (Benjamin and Ursell 1954; Miles 1984; Miles and Henderson 1990; Miles 1993; Bechhoefer and Johnson 1996; Müller et al. 1997; Müller 1998; Mancebo and Vega 2002; Huepe et al. 2006; Périnet et al. 2009, 2012) and experimentally (Douady 1990; Edwards and Fauve 1994; Bechhoefer et al. 1995; Kityk et al. 2002; Westra et al. 2003; Residori et al. 2007; Nguyem and Caps 2011) for the study of pattern formation. From an appropriate choice of the experimental parameters, several distinct patterns can be observed, consisting of a set of ordered geometrical figures like stripes, squares, triangles, and hexagons. Superlattice patterns Kudrolli et al. (1998) and localized structures Arbell and Fineberg (2000, 2002) have also been observed using two-frequency forcings. Understanding the types of patterns that form is challenging. The threshold for instability and the observed patterns depend on the fluid's viscosity and surface tension, the forcing acceleration Γ, and the shape and size of the vessel. In addition, fluctuations in the frequency and amplitude of the driving force may bring an existing pattern to a mixed state with a fraction of spatiotemporal chaos (Kudrolli and Gollub 1996). In the limit of weak dissipation, the results of classical Faraday experiments have mostly been understood on the basis of linear analyses (Müller 1998) for a spatially infinite liquid bath. Moreover, the mechanisms of pattern selection have been investigated using the tools of symmetry and bifurcation theory (Silber et al. 2000; Skeldon and Guidoboni 2007). Numerical simulations, involving the solution of the Navier–Stokes equations coupled to a front-tracking method for treatment of the free surface, have also started to appear by assuming that the liquid surface is perfectly flat at the edge of the lateral walls where no-slip boundary conditions apply (Périnet et al. 2009). However, these do not account for realistic experiments where the meniscus dynamics is important (Douady 1990). In particular, for small-size containers a strong coupling exists between the capillary waves generated by the meniscus and the Faraday waves (Nguyem and Caps 2011).

Whereas traditional experiments on Faraday wave patterns refer to single containers of varied sizes and shapes, Delon et al. (2010) observed the formation of regular patterns in the case where the liquid–air interface was split over a network of square cells. This kind of experiments has been found to have potential applications for the detection and location of liquids in internal cavities of cellular–core sandwich structures employed in mechanical and aeronautical constructions. Usually, the cells are made to define a regular grid and may have different geometries, the most commonly employed being of hexagonal shape so that the cellular structure resembles a beehive honeycomb. A long-standing problem, which is also considered to be a major defect of the structure, is the presence of liquid in the cells. Apart from different existing methods, one promising technology to locate where the liquid is and quantify its amount is based on inducing Faraday waves on the surface of the liquid by means of an excitation wave generation device (David et al. 2010). The dynamics representative of the wave patterns that arise in regular cell networks are also of help to understand the assembly patterns of cell spheroids in the bioengineering of three-dimensional tissue and organoid constructs, where a recently developed technology has shown that initially randomly distributed cell spheroids in a vibrated fluidic environment assemble into predefined patterns at the nodes of standing waves (Chen et al. 2015). This way, assembly patterns of cell spheroids of different symmetric modes can be predicted by the corresponding wave functions.

In the experiments of Delon et al. (2010), after a transient state, just above the Faraday threshold, neighbor cells are seen to collaborate synchronously to form a liquid peak at their common intersections, giving rise to a regular square lattice over the entire network for exciting frequencies in the range between 10 and 16 Hz. Similar experiments conducted by Peña-Polo et al. (2014) over a network of small equilateral triangular cells have shown that changing the grid geometry from square to triangular adds an extra degree of freedom for wave interaction, doubling the number of patterns that form and extending the range of frequencies ($10 \leq F \leq 28$ Hz) for which collective cell behavior is observed.

In particular, whereas Delon et al. (2010) experiments provide only a limited and qualitative view of the parametrically forced surface waves, here we (a) extend the range of frequencies (F) and amplitudes (A) of the driving force, (b) perform a finer sweep of the parameter space (A,F) to determine the regions that separate the synchronous formation of regular patterns from those where single oscillons form synchronously and where disordered wave fields appear within individual cells, (c) provide a quantitative picture of the parametrically excited waves in terms of a Pearson correlation analysis to determine their spectrum of mode frequencies, and (d) compare the experimental results with the traditional dispersion relation of free unforced waves and the dispersion relation of Faraday waves for

nonzero forcing and dissipation derived by Rajchenbach and Clamond (2015). Here, we deal only with a square cell network because of its simplicity and leave more complex geometries, as the triangular and hexagonal ones, for future studies.

2 Experimental setup

The experimental setup consists of a transparent acrylic vessel with a horizontal square base of size 25×25 cm^2 and height 5 cm fixed rigidly to the table of a TIRA TV51075 shaker that can deliver a maximum force of 75 N with peak-to-peak amplitude oscillation of 1 cm. A white styrene grid composed of 81 square cells of sides $l = 2.5$ cm and height $h = 1.5$ cm each is fixed to the bottom of the vessel. The cells are filled with distilled water doped with methylene blue up to a depth of $d = 0.7$ cm. All cells have at their bottom side a small circular hole of diameter 0.5 mm to ensure the same level of liquid over the entire grid. With these parameters, the total payload was ≈1.6 kg and the maximum allowed dimensionless peak-to-peak acceleration was $\Gamma \approx 4.55$.

The shaker is driven using a control software installed in a host computer from which we input a value of the amplitude, A, and frequency, F. The input frequency is received by a VR8500 controller connected to the computer, which generates an output sinusoidal signal. The output signal is amplified with a power amplifier and transmitted to the shaker. The amplitude is measured by means of a piezoelectric accelerometer fixed onto the shaker table and connected to the controller, which receives an oscillating voltage from the accelerometer and transforms it into a sinusoidal signal. The signal is checked to give the desired amplitude by a multifunctional data acquisition board and processed by the host computer, where a software is run to provide the oscillation amplitude in millimeters and the frequency in Hz. The quality of the acceleration was checked by measuring the calibrated signal from the accelerometer at frequencies in the range 10–22 Hz and peak-to-peak amplitudes from 0.2 to 6 mm. No discernible higher harmonics of the signals were observed from their power spectrum.

3 Experimental results

Patterns were visualized by light reflected from the liquid surface by a high-speed REDLAKE MotionXTRA HG-100K camera, which looks directly down onto the surface at a height of 80 cm from the vessel. Images were captured at a spatial resolution of 1504×1128 pixels. At this resolution, the videos were recorded at a speed of 1000 fps and exposition time of 525 μs for the measurements. A square array of four fluorescent 105 W lamps was mounted symmetrically for illumination at a height of 20 cm from the vessel. The integration time of the images ($=4.95 \times 10^{-4}$ s) is kept well below half the period of the waves, and hence they can be considered as instantaneous photographs of the surface. The images were processed and stored in a dedicated digital imaging system. To avoid modifications of the density, viscosity, and surface tension of water due to heating, the light bulbs were turned on only during video recording for no more than 10 s.

To determine the regions in the parameter space (A,F) where synchronized regular patterns form over the cell network, we have varied the excitation frequency and amplitude in the intervals $10 \le F \le 24$ Hz and $0.1 \le A \le 3$ mm, respectively. The dots in Fig. 1 mark the locus in the (A,F)-space of the experimental tests. The minimum frequency depicted in Fig. 1 corresponds to 10 Hz because below this frequency, the wavelength of the perturbations at the surface are larger than the cell size and so no excitation of the liquid surface is observed. Just above 10 Hz, the wavelengths become comparable to the length of the cell diagonals ($l_d \approx 3.53$ cm) and, after a transient state, adjacent cells progressively synchronize to form a regular pattern over the whole grid (Delon et al. 2010). For forcing frequencies in the range $10 \le F \le 18$ Hz, the maximum amplitude was set to 3 mm, while at higher exciting frequencies the maximum amplitude was lowered to about 2 mm (for $F = 24$ Hz) in order not to exceed 60% of the shaker's stroke capability. Each experiment (marked by a dot in Fig. 1) was repeated up to five times to assess the reproducibility of the observed patterns for the given amplitude and frequency of the forcing.

In a network of interconnected cells of small size, as the one employed here, the effect of the capillary menisci at the cell walls plays an important role. For instance, the external forcing induces the characteristic height of the menisci to evolve according to the relation (Douady 1990)

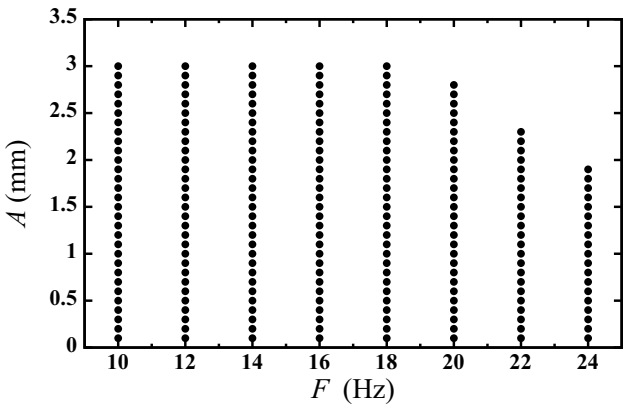

Fig. 1 Locus in the (A,F)-space of the experimental tests

$$h_m(t) = \left[\frac{\sigma}{\rho g(t)}\right]^{1/2}, \quad (2)$$

where σ is the surface tension of the liquid, ρ its density, and $g(t)$ the modulated gravitational acceleration defined by Eq. (1). Equation (2) is the instantaneous capillary length. In the absence of forcing, i.e., when $g(t) = g$, it just defines the capillary length, l_c. Accordingly, the time variation of the meniscus height generates capillary waves, which dissipate by viscous shear and interact with the Faraday waves excited subharmonically. In small-size containers, the coupling between the meniscus and the Faraday waves is strong, inducing a stabilizing effect on the liquid surface (Nguyem and Caps 2011), and so more energy is required to excite Faraday waves than in large recipients or unbounded fluids. Preliminary tests in the laboratory have shown that when the cell walls are coated with Teflon tape, the height of the meniscus is considerably reduced and an almost flat air/liquid interface is observed at contact with the solid walls, i.e., the wetting angle becomes ≈90°.

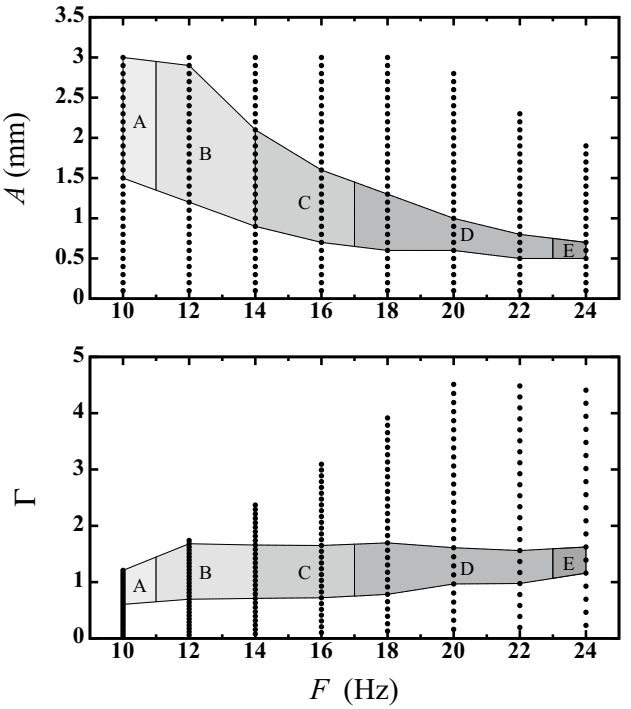

Fig. 2 Amplitude (*top*) and dimensionless acceleration (*bottom*) of the forcing oscillations as functions of the exciting frequency. The *gray-toned areas* show the experimentally determined regions where regular patterns form as a result of the collective behavior of neighboring cells (*A* and *B*), where localized oscillons arise within individual cells forming an ordered matrix (*C* and *D*), and where disordered periodic wave patterns are seen within each individual cell (*E*)

Regularly distributed bumps of liquid are formed at the cell intersections for forcing frequencies in the range $10 \le F < 14$ Hz. Figure 2 (top) shows the regions (A and B) in the (A,F)-space where such symmetric patterns appear. The same is also depicted in terms of the acceleration amplitude, Γ, of the forcing oscillations (bottom). Two different modes are observed. A square lattice of bumps forms for $10 \le F \le 11$ Hz as shown in the top view images of Fig. 3, corresponding to region A in Fig. 2. If the driving force is maintained, the same pattern is recurrently repeated with alternation of the peaks occurring at the grid nodes at twice the network scale every half a period, as we may see by comparing the two images of Fig. 3. In this case, neighbor cells arranged in a square-like distribution collaborate synchronously to form a well-defined bump at their common node by sharing nearly all of their liquid content. The dynamics observed in Fig. 3 is representative of the wave patterns that arise near the transition when the forcing exceeds the Faraday threshold. Synchronization is due to cell waves interacting diagonally and converging at grid nodes. A similar collective behavior was also observed at higher exciting frequencies in the range $11 < F < 14$ Hz, but this time tilted by 45° with respect to the grid orientation as shown in Fig. 4, corresponding to region B in Fig. 2. We may see that as the forcing frequency is increased, the amplitude range for which these regular patterns appear decreases. Similar patterns were reported by Delon et al.

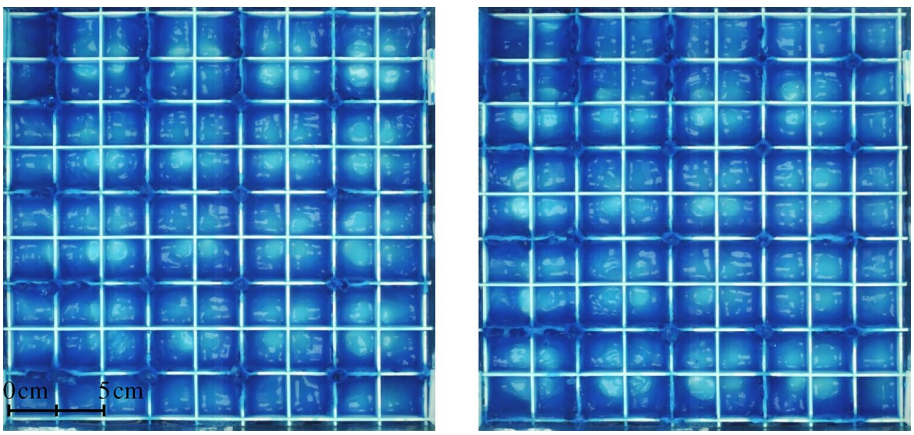

Fig. 3 *Top view images* of the resulting pattern for $F = 10$ Hz, amplitude $A = 2.0$ mm, and acceleration $\Gamma = 0.81$. Bumps of liquid form at the nodes of adjacent cells at the dual vertical and horizontal network scale. Both photographs are separated by half a wave period, showing alternation of the bump positions in the grid

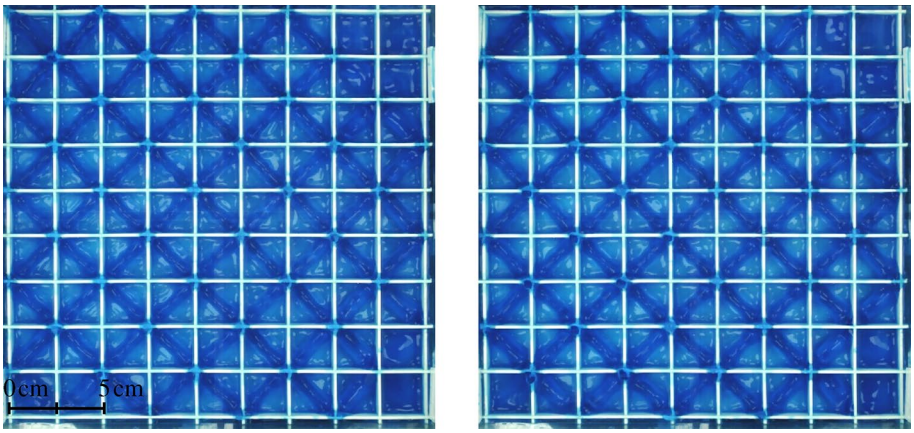

Fig. 4 *Top view images* of the resulting pattern for $F = 12$ Hz, amplitude $A = 1.3$ mm, and acceleration $\Gamma = 0.75$. A square lattice is formed again but now tilted by 45° at the network scale. Both photographs are separated by half a wave period, showing alternation of the bump positions in the grid

(2010) for the frequency intervals $10 \leq F \leq 12$ Hz and $12 < F \leq 16$ Hz, respectively, using square cells of higher height (2.5 cm) and filled with liquid up to a height of 1.3 cm.

At $F = 14$ Hz, two different patterns coexist simultaneously, corresponding to a mixed state as shown in Fig. 5 for $A = 1.2$ mm and $\Gamma = 1.26$. On the left part of the grid, oscillons are formed at the center of individual cells, while a regular lattice of bumps as the one shown in Fig. 4 is formed on the right part. When the experiment was repeated with identical parameters and conditions the same mixed state was reproduced. Evidently, $F = 14$ Hz corresponds to a transition frequency. Changing the driving amplitude at this frequency causes the patterns to be mixed differently over the grid. At even higher frequencies in the interval $14 < F \leq 23$ Hz, the wavelength of the driving oscillations becomes either comparable or smaller than half the cell diagonals and so collective behavior is no longer seen because the waves remain trapped within individual cells, forming localized oscillons at their approximate centers (regions C and D in Fig. 2). The difference between these regions lies on the way the oscillons are formed within the cells. In region C, an oscillon arises because the liquid in a cell converges radially to its center, while in region D the same occurs because of wave interaction only along the diagonals of a cell. Compared to regions A and B, localized oscillons are observed for a wider range of driving frequencies. However, as the driving frequency increases, the range of amplitudes for which oscillons form becomes progressively shorter. The top views of Fig. 6 shows an ordered matrix of oscillons for $F = 16$ Hz, $A = 1.0$ mm, and $\Gamma = 1.03$. Oscillons of opposite polarity are seen in a few cells on the right part of the grid. This inversion of polarity was observed for all driving parameters falling within regions C and D, with the distribution of up and down oscillons varying rather irregularly with the driving frequency and amplitude. No obvious correlation between the grid fraction occupied by oscillons with inverted polarity and the driving parameters could be established from the present experiments.

At $F > 23$ Hz, a disordered pattern is observed within each cell (region E in Fig. 2). Figure 7 shows the top view images of the grid for $F = 24$ Hz, $A = 0.7$ mm, and $\Gamma = 1.624$. The wave field in all cells looks random and is dominated by oscillating blobs approximately a quarter of the cell size in diameter. Although the number of blobs per

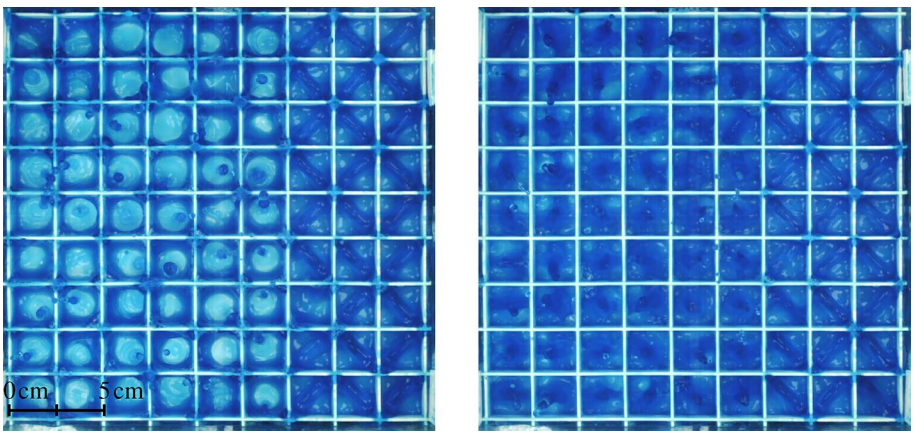

Fig. 5 *Top view images* of a mixed pattern formed at $F = 14$ Hz, amplitude $A = 1.2$ mm, and acceleration $\Gamma = 1.26$. A matrix of localized oscillons appears on the *left part* of the grid mixed with a regular pattern of bumps on the *right part*. The oscillons alternate their polarity synchronously with the bump positions every half a period as can be seen by comparing both photographs

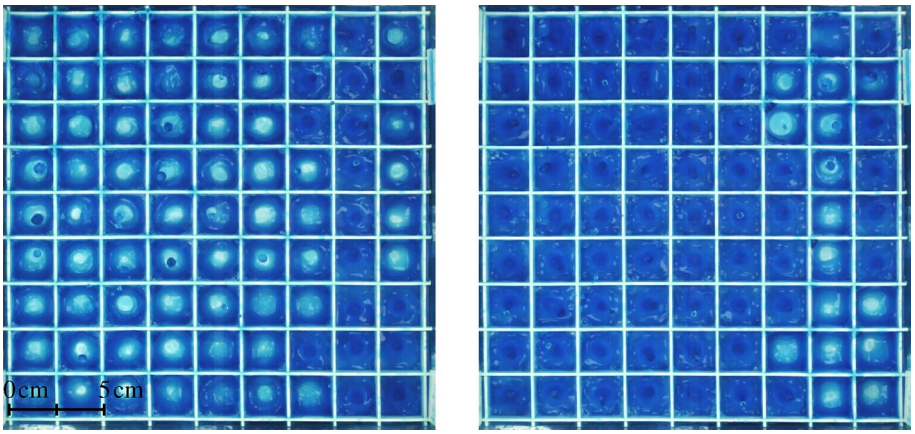

Fig. 6 *Top view images* of the resulting pattern for $F = 16$ Hz, amplitude $A = 1.0$ mm, and acceleration $\Gamma = 1.03$. Localized oscillons at the approximate centers of individual cells are formed. Oscillons of opposite polarity are seen in some cells on the *right*. Alternation of the polarity occurs every half a period as can be seen by comparing both photographs

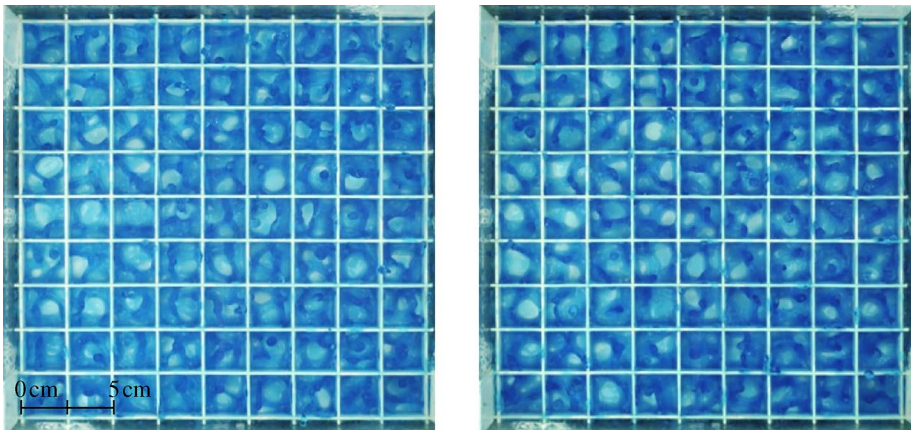

Fig. 7 *Top view images* of the resulting pattern for $F = 24$ Hz, amplitude $A = 0.7$ mm, and acceleration $\Gamma = 1.624$. A random wave field consisting of oscillating blobs forms within each individual cell. The blobs invert their polarity approximately every half a period as can be seen by comparing both photographs

cell is never greater than three in our case, the observed wave field resembles the water surface ripples observed by Shats et al. (2012), who interpreted them as made of oscillons interacting on the capillary–gravity range (Miles and Henderson 1990; Perlin and Schultz 2000). The blobs in Fig. 7 are seen to move randomly on the surface, and in many cases they collide and merge with their companion blobs. However, the frequency spectrum of the surface gradient is not random, but consists of spectrally broadened harmonics with frequencies $f_n = nF/2$ for $n = 2, 4, \ldots$ (Shats et al. 2012).

The best fits to the upper and lower amplitude curves bounding the regions A–E in Fig. 2 are given with a coefficient of determination $R^2 = 1$ by the fourth degree polynomials

$$A^+(F) = 3.0 \times 10^{-5} F^4 - 2.5 \times 10^{-3} F^3 + 0.0945 F^2 - 1.7217 F + 13.836, \quad (3)$$

$$A^-(F) = 9.0 \times 10^{-6} F^4 - 8.0 \times 10^{-4} F^3 + 0.0304 F^2 - 0.5611 F + 4.7093, \quad (4)$$

respectively. For all driving amplitudes and frequencies below $A^-(F)$, the resulting forcing Γ is not enough to produce appreciable deformations of the liquid surface, while highly disordered wave fields were observed for all amplitudes and frequencies above the curve $A^+(F)$. In this latter case, pronounced liquid spikes arose from the liquid surface accompanied by pinching and ejection of small drops from each cell in all directions. A detailed comparison of the wave fields over the grid has shown that in all cases, the resulting patterns were different from cell to cell. As was pointed out by Shats et al. (2012), a seemingly chaotic state on the water surface can be turned into ordered matrices of oscillons by just reducing their mobility via the addition of a viscous solution. At higher frequencies, we have separated this chaotic region from region E based on the fact that in the latter case the disordered wave field was never accompanied by pinching and/or ejection of liquid from the cells.

As mentioned previously, in the present experiments the liquid bumps form two different patterns of square lattices for frequencies in the range $10 \leq F < 14$ Hz due to diagonal wave interaction between adjacent square cells. For comparison, previous experiments using a triangular cell network with cells of sides 2.5 cm and depth 1.5 cm each, filled with colored distilled water up to a height of 0.7 cm, have shown the formation of four

different patterns between 10 and 28 Hz (Peña-Polo et al. 2014). The increased number of patterns in these experiments is due to an extra degree of freedom available for wave interaction in a triangular cell, i.e., the three altitudes in a triangle against the two diagonals of a square. Evidently, the number and nature of the patterns that form as well as the frequency ranges for which collective behavior between adjacent cells is observed strongly depend on the grid geometry. Unfortunately, a quantitative comparison between both types of experiments is not possible because a waveform correlation analysis for the triangular data is not available.

4 Discussion of results

4.1 Waveform correlation analysis

A waveform analysis was performed by processing all recorded videos, pertaining to the forcing parameters falling within regions A–E in Fig. 2, using a Pearson correlation of the time series of photographs composing each video. To get information about the waveforms, we first calculate the correlation coefficient as a function of time by correlating the set of images corresponding to the first wave period to those corresponding to subsequent wave periods in the video. The two-dimensional correlation coefficients constructed this way provides a measure of the differences between the first set of photographs with all successive ones contained in the video. The resulting power spectrum is generated by computing the fast Fourier transform (FFT) of the two-dimensional correlation array. The power spectra from the video processing of subsequent trials of the same experiment were seen to overlap in all cases considered, implying that the patterns shown in Figs. 3, 4, 5, 6 and 7 are indeed quite robust.

The resulting waveforms (top) and power spectra (bottom) corresponding to the experiments of Figs. 3, 4, and 6 are shown in Figs. 8, 9, and 10, respectively. The peaks in Figs. 8 and 9 have $C \approx 0.8$, meaning that the strength of the correlation between the liquid bumps in the regular lattices of Figs. 3 and 4 is moderately high. In contrast, the wave valleys look noisy and are poorly correlated ($C < 0.2$). Physically, they represent the instants when the cells become almost depleted of liquid. The low correlation is due to the amount of depletion not being exactly the same in all cells in space and time, while the noise is produced by the vibration of the remnant liquid attached to the walls and bottom of some cells. The waveform in Fig. 10 corresponds to the experiment of Fig. 6, where an ordered matrix of oscillons forms at a forcing frequency of 16 Hz. Compared to Figs. 8 and 9, all peaks are not at the same height and the data show a moderate positive correlation,

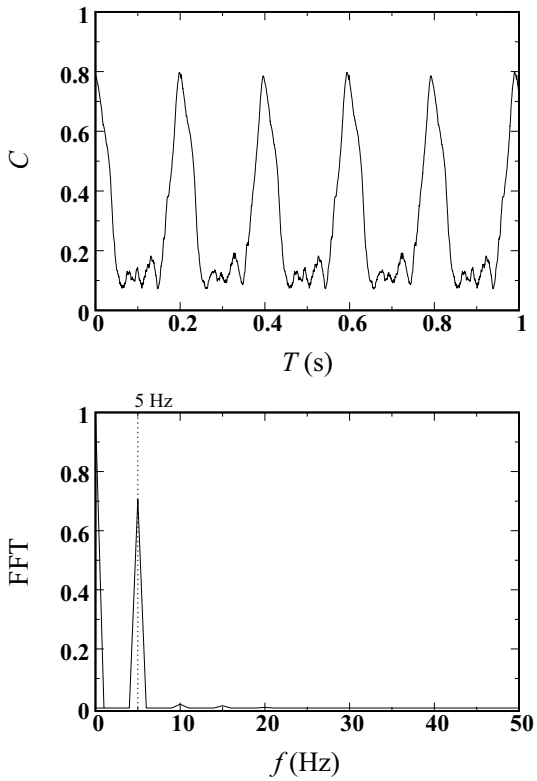

Fig. 8 Pearson correlation coefficient as a function of time showing the correlated waveform for the regular lattice of Fig. 3 (*top*) and the corresponding frequency spectrum as calculated from the fast Fourier transform of the temporally varying correlation coefficient (*bottom*). For these forcing parameters, the wave period is ≈0.198 s and the maximum frequency peak is at $f = 5$ Hz, corresponding exactly to half the forcing frequency $F = 10$ Hz for this experiment

implying that not all oscillons in the matrix reach the same altitude and have the same liquid content due to nonlinear effects. In all cases, the standing waves are periodic and the periodicity decreases with increasing forcing frequency, F, consistently with the capillary–gravity wave dispersion relation. The bottom plot in each figure displays the frequency spectrum of the wave signals. The dominant response frequency always occurs at half the driving frequency, i.e., $f = F/2$, corresponding to the first resonance condition ($n = 1$) (Benjamin and Ursell 1954; Miles 1993; Douady 1990). A second peak of lower strength occurs at $f = F$, corresponding to the first harmonic ($n = 2$). In most cases, higher harmonics with $n = 4, 6, \ldots$ are either extremely weak or even not present. The high peaks to the left of the power spectra (around $f = 0$) are spurious and not present in the input. They appear in the frequency spectrum because the FFT was performed on waveforms that possess end-point discontinuities and that do not contain a whole number of periods as can be seen from the top plots of Figs. 8, 9, 10 and 11. Therefore, the FFT evaluates these waveforms with an end-point error and generates a power

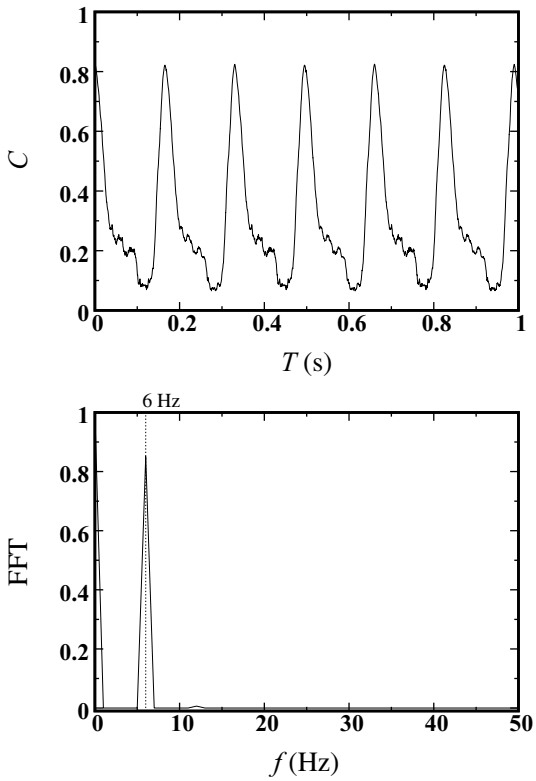

Fig. 9 Same as in Fig. 8, but with the regular lattice of Fig. 4. The wave period is ≈0.166 s and the maximum frequency peak is at $f = 6$ Hz, corresponding to half the forcing frequency $F = 12$ Hz for this experiment

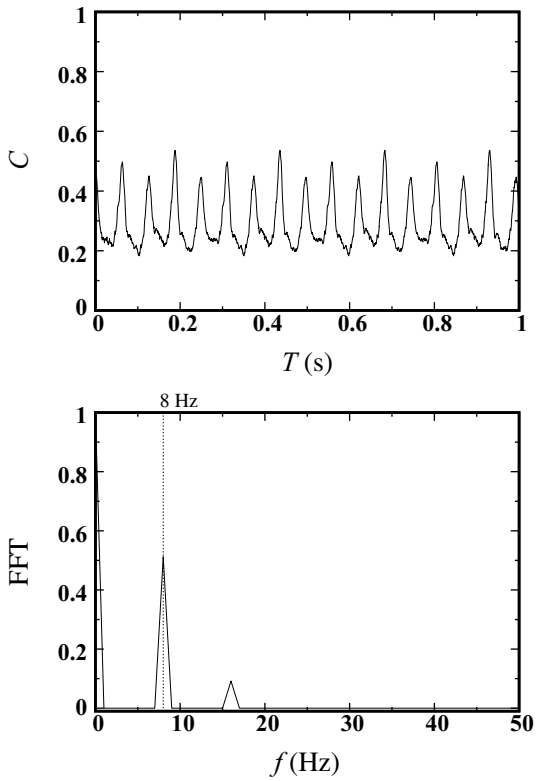

Fig. 10 Same as in Figs. 8 and 9 for the ordered matrix of oscillons shown in Fig. 6. The wave period is ≈0.063 s and the maximum frequency peak is at $f = 8$ Hz, corresponding to half the forcing frequency $F = 16$ Hz for this experiment. The second peak at $f = F = 16$ Hz corresponds to the first harmonic response ($n = 2$)

spectrum containing false frequency components representative of the end-point mismatch.

The correlated waveform and corresponding frequency spectrum of the random wave field of Fig. 7 are shown in Fig. 11. The motion is periodic and the strength of the correlation is moderately high, showing harmonic responses $f_n = nF_n/2$ for $n = 2$ and $n = 4$. At these higher frequencies, quasistanding waves are found to coexist with a spatially extended fluid transport. More specifically, it was recently demonstrated by Francois et al. (2014) that the ordered–disordered transition in Faraday waves from a lattice of vertically oscillating solitons to a complex fluid motion, whose statistics is similar to that of two-dimensional turbulence, is due to the generation of vorticity in the horizontal flow by the oscillons themselves at their size scale. As this horizontal energy is spread over a range of scales by the Kolmogorov–Kraichnan inverse energy cascade, the interaction among these vortices explains how quasistanding waves may fuel two-dimensional turbulence. Although Francois et al. (2014) experiments refer to a single circular container, the wave-field topography observed within individual cells in our experiments for $F > 23$ Hz (region E in Fig. 2) is remarkably similar to the disordered patterns seen in their experiments. Therefore, as they claimed, two-dimensional Navier–Stokes turbulence may well be a source of disorder in Faraday waves.

4.2 Comparison with theory

For parametrically driven infinitesimal surface waves, the surface deformation, $\zeta = \zeta(\mathbf{k}, t)$, is described by the damped Mathieu equation (Benjamin and Ursell 1954)

$$\zeta_{tt} + 2\Sigma\zeta_t + \omega_0^2[1 - \Gamma\cos(\Omega t)]\zeta = 0, \tag{5}$$

where $\mathbf{k}$ is the wavevector ($k = |\mathbf{k}|$), $\Sigma = \Sigma(k)$ is the attenuation due to viscous dissipation and friction, and $\omega_0 = \omega_0(k)$ is the angular frequency of linear waves without damping and forcing. For capillary–gravity waves, ω_0 is given by

$$\omega_0^2 = \left(gk + \frac{\sigma k^3}{\rho}\right)\tanh(kd), \tag{6}$$

while the dimensionless forcing is

$$\Gamma = \rho\Omega^2 A\left(\rho g + \sigma k^2\right)^{-1}, \tag{7}$$

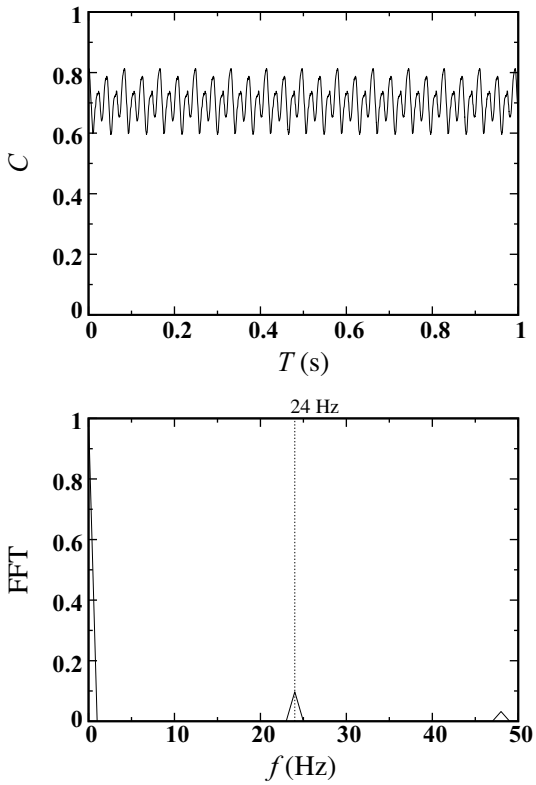

Fig. 11 Same as in Figs. 8, 9, and 10 for the disordered wave patterns observed in Fig. 7. The wave period is ≈0.021 s and this time the surface waves are harmonic with the maximum frequency response ($n = 2$) at $f = F = 24$ Hz. A second peak occurs at the second harmonic ($n = 4$, $f = 2F = 48$ Hz)

where σ and ρ are, respectively, the surface tension and density of the liquid, and d is the liquid depth. For $kd \gg 1$, $\tanh(kd) \to 1$ and Eq. (6) gives the linear dispersion equation for deep water. Converting Eq. (5) into the undamped Mathieu equation

$$\eta_{\tau\tau} + \left[p - 2q\cos(2\tau)\right]\eta = 0, \tag{8}$$

through the changes of variables $t \to \tau = \Omega t/2$ and $\zeta \to \eta = \zeta(\mathbf{k}, t)\exp(\Sigma t)$, where $p = 4(\omega_0^2 - \Sigma^2)/\Omega^2$ and $q = 2\Gamma\omega_0^2/\Omega^2$, Rajchenbach and Clamond (2015) have recently demonstrated that the Floquet exponent, $\mu(p, q)$, in the aperiodic solutions of Eq. (8), which correspond to periodic solutions of Eq. (5), obeys the relation

$$\mu(p,q) = \mathrm{Re}(\mu) + i\mathrm{Im}(\mu) = \frac{2\omega}{\Omega} + i\frac{2\Sigma}{\Omega} = n + i\frac{2\Sigma}{\Omega}, \tag{9}$$

which establishes an implicit dispersion equation relating the wavenumber k and the angular frequency $\omega = n\Omega/2$ for Faraday waves via ω_0, Γ, and Σ. As was noted by Rajchenbach and Clamond (2015), the key point here is that $\omega = 2\pi f_n = n\Omega/2$ is the actual wave angular frequency and not ω_0, as is often assumed in analyses of Faraday waves. Indeed, ω_0 is the angular frequency of unforced, undamped waves for which $\Gamma = \Sigma = 0$, while Eq. (9) is the actual dispersion relation of Faraday waves for nonzero forcing and dissipation.

Using a weakly nonlinear model, Rajchenbach and Clamond (2015) also demonstrated that the rest state is unstable if $\Gamma > \Gamma_c$, where

$$\Gamma_c = 4\left[\left(1 - \frac{\omega_0}{\omega}\right)^2 + \left(\frac{\Sigma}{\omega}\right)^2\right]^{1/2}, \tag{10}$$

is the minimum forcing necessary to destabilize the rest state and generate surface waves. Thus, when $\Gamma > \Gamma_c$ the rest state becomes unstable through a supercritical transition for short waves. In this expression, ω_0 and Γ are related to k through Eqs. (6) and (7), respectively. For a finite liquid depth as is the case in the present experiments ($d = 0.7$ cm), the attenuation factor in the limit of small viscosities can be approximated by Hunt (1964)

$$\Sigma(k) = \nu k^2\left[2 + \frac{\coth(2kd)}{\sinh(2kd)}\right] + \frac{2kd}{\sinh(2kd)}\left(\frac{g^{1/2}\nu k}{8d^{3/2}}\right)^{1/2}, \tag{11}$$

where ν is the kinematic viscosity of the liquid. The first term on the right-hand side of Eq. (11) is the contribution of bulk dissipation, while the second term is the attenuation due to friction with the bottom. Using Eqs. (6), (7), and (11), Eq. (10) can be written in terms of the critical wavenumber k_c as

$$(\rho g + \sigma k_c^2)^2\mathcal{F}(k_c) - \pi^3 F^3 \rho A = 0, \tag{12}$$

where

$$\mathcal{F}(k_c) = \Sigma^2(k_c) + \left(gk_c + \frac{\sigma k_c^3}{\rho}\right)\tanh(k_c d) - 2\pi F\left[\left(gk_c + \frac{\sigma k_c^3}{\rho}\right)\tanh(k_c d)\right]^{1/2} + \pi^2 F^2. \tag{13}$$

Taking $\rho = 998.2$ kg m^{-3}, $\nu = 1.0034 \times 10^{-6}$ m^2 s^{-1}, and $\sigma = 7.275 \times 10^{-2}$ kg s^{-2} for the density, kinematic viscosity, and surface tension of water at 20 °C, Eq. (12) predicts wavelengths between $\lambda_c \approx 3.87$ and ≈4.33 cm for $1.5 \le A \le 3$ mm and $F = 10$ Hz. For the same amplitude range and $F = 11$ Hz, the critical wavelengths are in the interval between ≈3.37 and ≈3.82. Within the margin of error implied by the weakly nonlinear approximation, these values are actually close to the length of the cell diagonals ($l_d \approx 3.53$ cm) below which Faraday waves are excited in the experiments. At lower forcing frequencies for $1.5 \le A \le 3$ mm, Eq. (12) yields wavelengths larger than ≈4.50 cm for $F = 9$ Hz so that no deformations of the water surface are visible. For $F = 14$ Hz, where a transition occurs from regular square patterns to ordered matrices of

oscillons, the predicted wavelengths are close to half the cell diagonals (≈1.8 cm). For $F > 14$ Hz, the predicted wavelengths become smaller than half the cell diagonals and therefore the waves remain constrained within individual cells.

For capillary–gravity waves with no attenuation, the dispersion relation is given by Eq. (6) with $\omega_0 \to \omega = \pi F$. In contrast to Eq. (12), the critical wavelengths are now independent of the forcing amplitude. The solution of Eq. (6) predicts wavelengths larger than Eq. (12) for all frequencies. For instance, at $F = 10$ Hz the predicted wavelength is $\lambda_c \approx 4.96$ cm, which is larger than the size of the cells for excitation of subharmonic waves. Only for $F = 14$ Hz does the wavelength become ≈3.42 Hz, implying a shift from the experimental minimum driving frequency of about 4 Hz. Even for $F = 23$ Hz, Eq. (6) yields $\lambda_c \approx 2$ cm, which is still larger than half the length of the cell diagonals. Thus, we may then conclude that compared to Eq. (6) the weakly nonlinear theory of Rajchenbach and Clamond (2015) is predicting fairly well the bifurcation from rest as well as the transition frequency from a regular pattern to ordered oscillons within individual cells, yielding a minimum driving frequency of ≈11 Hz against 10 Hz for the experiments and a transition frequency very close to the experimental value of 14 Hz. However, considering that the present Faraday wave experiments are rather far from traditional, it would be necessary to validate the above conclusions against more classical experiments.

5 Conclusions

We have reported experimental observations of the Faraday instability in a network of small square cells filled with water for forcing frequencies and amplitudes in the intervals $10 \le F \le 24$ Hz and $0.1 \le A \le 3$ mm, respectively.

The minimum driving frequency for which periodic surface waves are excited over the cell network corresponds to 10 Hz, because below this value the wavelengths of the perturbations at the surface become larger than the cell size and so no surface waves are observed. Square lattice patterns arise for driving frequencies in the interval $10 \le F < 14$ Hz. After a transient state, adjacent cells experience a synchronized collective behavior where cell waves interact diagonally and converge at grid nodes, forming a square lattice of liquid bumps in much the same way as described by Delon et al. (2010). Recurrent alternation of the bumps is seen to occur every half a period at twice the network scale. At higher forcing frequencies in the range $14 < F \le 23$ Hz, collective behavior is no longer observed as the waves remain trapped within individual cells, forming localized oscillons at their approximate centers and giving rise to a matrix of ordered oscillons over the entire grid. We demonstrate that for such regular patterns, wave motion within individual cells is highly correlated with a dominant response frequency corresponding exactly to $f = F/2$. Other minor peaks in the frequency spectra were found to coincide with harmonic response frequencies $f_n = nF/2$ for $n = 2, 4, \ldots$ However, in many, if not in most cases, the only relevant harmonic frequency occurs for $n = 2$, with the other harmonics being negligible or even not present.

At frequencies $F > 23$ Hz of the driving force, a disordered wave pattern is observed within individual cells for a narrow range of forcing amplitudes between 0.5 and 0.7 mm. At amplitudes higher than 3 mm for $F = 12$ Hz and 0.7 mm for $F = 24$ Hz, a region is encountered in the (A,F)-space, where surface waves converge within individual cells to produce liquid spikes accompanied by pinching and ejection of small drops from the cells in all directions. An analysis of such chaotic states escapes from the aim of this study and will be considered in a forthcoming paper. In the former case, the wave field looks random and is dominated by oscillating blobs approximately a quarter of the cell size in diameter. The surface topography resembles the water surface ripples observed by Shats et al. (2012), who interpreted them as made of oscillons interacting on the capillary–gravity scale with the frequency spectrum of the surface gradient being not random and consisting of spectrally broadened harmonics $f_n = nF/2$ (with $n = 2, 4, \ldots$). While in their case, the dominant response frequency was subharmonic ($f = F/2$), in our experiments the maximum response is harmonic with $f = F$ ($n = 2$). For experiments similar to those of Shats et al. (2012), Francois et al. (2014) demonstrated that the source of disorder is due to Navier–Stokes two-dimensional turbulence fueled by the interaction of vortices in the horizontal flow as generated at the oscillons' scale by their up and down motions. While this interesting scenario may well explain the ordered–disordered transition in Faraday waves and how quasistanding waves may fuel two-dimensional turbulence, it could also provide a different pathway to interpret the disordered–chaotic transition when the liquid is submitted to large forcing amplitudes.

As a final remark, the experimentally determined minimum forcing necessary to destabilize the rest state and generate surface waves was found to be consistent with predictions from a weakly nonlinear stability analysis of stationary solutions as derived from the dispersion relation of Faraday waves with nonzero forcing and dissipation (Rajchenbach and Clamond 2015). Moreover, a few experiments have shown that varying the depth of the liquid affects the strength of the forming bumps and oscillons. Future work will be addressed to establish a correlation between the liquid content in the cells and the size of the liquid peaks. Further work in this line will also focus on studying the effects of changing the size, the geometry, and

the material of the cell network. In particular, reverting to a material which minimizes the extent of the meniscus would be of interest to uncouple the effects of the capillary waves induced by the meniscus dynamics from the Faraday waves in such small containers (Nguyem and Caps 2011).

Acknowledgements We thank the reviewers for a number of comments and suggestions that have improved the content of the manuscript. F. P.-P. acknowledges ABACUS for financial support during his visit to the Department of Mathematics of Cinvestav-IPN. This work was partially supported by the Departamento de Ciencias Básicas e Ingeniería (CBI) of the Universidad Autónoma Metropolitana–Azcapotzalco (UAM-A) through internal funds and by ABACUS through the CONACyT Grant EDOMEX-2011-C01-165873.

References

Arbell H, Fineberg J (2000) Temporally harmonic oscillons in Newtonian fluids. Phys Rev Lett 85:756–759

Arbell H, Fineberg J (2002) Pattern formation in two-frequency forced parametric waves. Phys Rev E 65:036224

Bechhoefer J, Ego V, Manneville S, Johnson B (1995) An experimental study of the onset of parametrically pumped surface waves in viscous fluids. J Fluid Mech 288:325–350

Bechhoefer J, Johnson B (1996) A simple model for Faraday waves. Am J Phys 64:1482–1488

Benjamin TB, Ursell F (1954) The stability of the plane free surface of a liquid in vertical periodic motion. Proc R Soc Lond A 225:505–515

Chen P, Güven S, Usta OB, Yarmush ML, Demirci U (2015) Biotunable acoustic node assembly of organoids. Adv Healthc Mater 4:1937–1943

David J, Vuong T-H, Roucaries B, Nogarede B, Crampagne R (2010) Method and device for detecting water in a cellular structure. Patent US 20,100,162,818 A1

Delon G, Terwagne D, Adami N, Bronfort A, Vandewalle N, Dorbolo S, Caps H (2010) Faraday instability on a network. Chaos 20:041103

Douady S (1990) Experimental study of the Faraday instability. J Fluid Mech 221:383–409

Edwards WS, Fauve S (1994) Patterns and quasi-patterns in the Faraday experiment. J Fluid Mech 278:123–148

Faraday M (1831) On a peculiar class of acoustical figures; and on certain forms assumed by a group of particles upon vibrating elastic surfaces. Philos Trans R Soc Lond 121:299–318

Francois N, Xia H, Punzmann H, Ramsden S, Shats M (2014) Three-dimensional fluid motion in Faraday waves: creation of vorticity and generation of two-dimensional turbulence. Phys Rev X 4:021021

Huepe C, Ding Y, Umbanhowar P, Silber M (2006) Forcing function control of Faraday wave instabilities in viscous shallow fluids. Phys Rev E 73:016310

Hunt JN (1964) The damping of gravity waves in shallow water. La Houille Blanche 6:685–691

Kityk AV, Wagner C, Knorr K, Müller HW (2002) Phase relaxation of Faraday surface waves. Phys Rev E 65(066304):066304

Kudrolli A, Pier B, Gollub JP (1998) Superlattice patterns in surface waves. Physica D 123:99–111

Kudrolli A, Gollub JP (1996) Localized spatiotemporal chaos in surface waves. Phys Rev E 54(2):R1052–R1055

Mancebo FJ, Vega JM (2002) Faraday instability threshold in large-aspect-ratio containers. J Fluid Mech 467:307–330

Miles JW (1984) Nonlinear Faraday resonance. J Fluid Mech 146:285–302

Miles J (1993) On Faraday waves. J Fluid Mech 248:671–683

Miles J, Henderson D (1990) Parametrically forced surface waves. Annu Rev Fluid Mech 22:143–165

Müller HW, Wittmer H, Wagner C, Albers J, Knorr K (1997) Analytic stability theory for Faraday waves and the observation of the harmonic surface response. Phys Rev Lett 78(12):2357–2360

Müller HW (1998) A perspective look at nonlinear media from physics to biology and social sciences. Lecture notes. In: Parisi J, Müller SC, Zimmermann W (eds) Physics, vol 503. Springer, Berlin, pp 45–60

Nguyem Thu Lam KD, Caps H (2011) Effect of a capillary meniscus on the Faraday instability threshold. Eur Phys J E 34:112–116

Peña-Polo F, Sánchez I, Sigalotti L Di G (2014) Faraday wave patterns on a triangular cell network. In: Sigalotti L Di G, Klapp J, Sira E (eds) Experimental and computational fluid mechanics with applications to physics, engineering and the environment. Springer, Berlin, pp 357–365

Périnet N, Juric D, Tuckerman LS (2009) Numerical simulation of Faraday waves. J Fluid Mech 635:1–26

Périnet N, Juric D, Tuckerman LS (2012) Alternating hexagonal and stripped patterns in Faraday surface waves. Phys Rev Lett 109(164501):164501

Perlin M, Schultz WW (2000) Capillary effects on surface waves. Annu Rev Fluid Mech 32:241–274

Rajchenbach J, Clamond D (2015) Faraday waves: their dissipation relation, nature of bifurcation and wavenumber selection revisited. J Fluid Mech 777:R2-1–R2-12

Residori S, Guarino A, Bortolozzo U (2007) Two-mode competition in Faraday instability. Europhys Lett 77:44003

Shats M, Xia H, Punzmann H (2012) Parametrically excited water surface ripples as ensembles of oscillons. Phys Rev Lett 108:034502

Silber M, Topaz CM, Skeldon AC (2000) Two-frequency forced Faraday waves: weakly damped modes and patterns selection. Physica D 143:205–225

Skeldon AC, Guidoboni G (2007) Pattern selection for Faraday waves in an incompressible viscous fluid. SIAM J Appl Math 67:1064–1100

Westra M-T, Binks DJ, van de Water W (2003) Patterns of Faraday waves. J Fluid Mech 496:1–32